從中子星的 X 射線推論出磁傾角與觀察角

卜宏毅

國立清華大學天文研究所

摘要

爲了研究造成射電脈衝星與射電波段沒有明顯可觀測訊號的中子星兩者不同的可能原因，我們推論出一些的射電訊號不明顯的中子星的磁軸傾角(α，中子星自轉軸和磁軸的夾角)和觀察者的觀察角(ζ，中子星自轉軸和觀察者視線方向的夾角)。針對具有 X 射線熱輻射的中子星，我們可以經由給定中子星表面的溫度分佈並假設中子星的表面輻射是以黑體輻射的形式描述，進而計算出模擬的光度曲線和光譜。再者，藉著改變模型中的 α 與 ζ 參數，並把觀測結果以及我們的計算結果與觀測結果相互比較，可以找出特定具有熱輻射性質的中子星所可能具有的 α 與 ζ 範圍。在計算中，我們考慮了廣義相對論造成的光徑彎曲以及重力紅移的效應。我們的結果顯示，沒有明顯的證據支持射電脈衝星與射電訊號不明顯的中子星兩者在 α-ζ 平面上的分佈有所不同。

Large Magnetic Inclination and Viewing Geometry of Neutron Stars Inferred from Their X-ray Emission

Pu Hung-Yi

Institute of Astronomy, National Tsing Hua University

Abstract

To investigate a possible reason of the difference between the radio-quiet neutron stars and radio pulsars, I constrained the possible ranges of magnetic inclination angle α and the observer's viewing angle ζ for several radio-quiet neutron stars with X-ray thermal emission. With a given surface temperature distribution of a neutron star and assuming the surface emission is described by Planck function, the model light curves and spectra were calculated. As α and ζ are parameters in the model, the possible range of these two angles for radio-quiet neutron stars can be inferred by comparing the computed flux and pulsed fraction with the observed ones. The calculation included photon path bending and gravitational redshift. The result shows no significant sign of the different distribution in the α-ζ plane for radio-quiet neutron stars and radio pulsars.

1   Introduction

A neutron star, a compact object with mass less than about three to five solar masses, is believed to be the debris after supernova explosions. From the theoretical point of view, several considerations are needed when deriving their properties because of their high mass-to-radius ratios (~0.2) and strong magnetic fields (~10^{12} Gauss). Information obtained form neutron star spectra greatly helps to understand their nature, such as the strength of the surface magnetic field, chemical composition of the neutron star surface, mass-to-radius ratio and surface gravity.

In observation, thousands of radio pulsars but few radio-quiet neutron stars (neutron stars with no significant detectable radio emission, e.x. Kaspi 2004, Popov 2003) have been discovered so far. If the radio emission indeed exists for all neutron stars and mainly come from the magnetic pole, therefore, the radio-quiet behavior of radio-quiet neutron stars may be the result of that the magnetic inclination angle (α) and the observer's viewing (ζ) angle prevent us from seeing the radio emission. However, samples of radio-quiet neutron stars with inferred α and ζ angle are few.

Thus, to investigate this point of view, it is helpful to develop a method to determine these angles of neutron stars with X-ray thermal emission because most of them are radio-quiet. Only Few (~20) neutron stars show thermal character in their spectra behavior. These sources include Anomalous X-ray Pulsars (AXPs) (e.x. Mereghetti et al. 2002), Soft Gamma Repeaters (SGRs) (e.x. Hurley 1999), X-ray dim isolated neutron stars (XDINs) (e.x. Haberl 2003, 2004), Central Compact objects (CCOs) (e.x. Pavlov et al. 2001) and some radio pulsars. Their spectra usually well fitted by Planck functions (plus power law). The relative soft thermal component may assigned to be cooling emission from the neutron star's surface while the relative hard thermal component may be caused by the thermal radia- tion from the polar hot spots on neutron star surface (Becker et al. 1997; Treves et al. 2000). On the other hand, isolated accreting old neutron stars (IONS) may also show thermal spectral component due to the ambient interstellar medium slow accretion into their polar caps (Treves et al. 2000).

By assuming surface thermal blackbody emission, I constructed model spectra and pulse profiles of emission from the whole surface of a neutron star (most the calculations are derived by Pechenick, Ftaclas and Cohen (1983), hereafter PFC), taking into account photon path bending, surface temperature distribution and the limb-darkening effect.

Neutron stars with spectral X-ray thermal components provide possibilities to infer their geometry. The idea is to find the consistent α and ζ angles, which can produce similar flux and pulse fraction similar to those in observation. The fitting temperatures of thermal spectral components in relative soft and hard X-ray band (the "TS" and "TH" component, respectively) can be viewed as the temperature of the hot polar cap and the neutron star surface, respectively. I con- strained the possible inclination angles and

viewing angles for several radio-quiet neutron stars with X-ray thermal emission by comparing the computed flux and pulsed fraction with the observed ones (The idea can been seen in the paper of Chang (2001)).

This paper is arranged as follows: Calculations of model spectra and model light curves are introduced in section 2; Section 3 presents the process and results of determining the α and ζ angles for several radio-quiet neutron stars. Finally, summary is in section 4.

2　Modeling the spectra and light curves of surface emission from neutron stars

2.1　Assumptions

The calculations are based on following assumptions:

1. The star is spherical symmetry. The metric outside the star is taken to be the Schwarzschild metric with mass M and radial coordinate r, and ignore the "dragging of inertial frame".

2. The surface of the star is at r = R, where R is the neutron star radius, with R/M > 3 (use geometry unit), so the star is larger than its "photon sphere". The observer is taken to be stationary at r = r_0 where $r_0 \to \infty$.

3. The region r < R is totally opaque, the region r > R is totally transparent.

4. The emission from the surface of the star is similar to blackbody radiation with some modified, i.e. For a specified region on the stellar surface:

$$I_v = f \times B_v$$

where I_v is the emission intensity form star surface, f is the modify function, which I will mention below, and $B_v = \frac{2v^2}{c^2} \frac{hv}{\exp^{hv/kT}-1}$, the Planck function.

5. The magnetic field on the star surface is a dipole form in the Schwarzschild curved space-time, $\vec{B}_{curr}$, which equals to

$$-\frac{3}{2}\frac{\mu_p \cos\theta_{mag}}{M^2 R}\left[\frac{R}{2M}\ln(1-\frac{2M}{R})+1+\frac{M}{R}\right]\hat{r}$$

$$+\frac{3}{2}\frac{\mu_p \sin\theta_{mag}}{M^2 R}\left[(\frac{R}{2M}-1)\ln(1-\frac{2M}{R})+1-\frac{M}{R}\right]\times(1-\frac{2M}{R})^{1/2}\hat{\theta}$$

which has been formulated by Wasserman and Shapiro (1983), where θ_{mag} is the angle between the magnetic axis and the surface normal, μ_p, which equals to $B_p R^3/2$, is the magnetic dipole moment, B_p is the magnetic field at pole.

2.2　Observed flux and light curves

The calculation of observed flux and light curves are derived in PFC's paper (their equations (3.9), (3.10) and (4.1).) In this paper, I define α as the angle between the rotation and the magnetic axes of the neutron star (β for PFC's notation); ζ is the angle between the axis of rotation and the observer's line of sight (γ for PFC's notation). θ_{obs}, the angle between the magnetic axes and the line of sight. Note, in my calculation,

$I_v(R,\theta,\varphi)=f \times B_v(T(R,\theta,\varphi))$,

and the model spectrum can be numerical calculated if the temperature distribution of the neutron star surface, $T(R,\theta \varphi)$, is given.

2.3　Limb-darkening

The effects of a strong magnetic field on neutron stars are twofold:

1. Anisotropy of the surface temperature distribution.

2. Magnetic beaming.

However, the magnetic beaming pattern is different everywhere because of the different magnetic field direction on neutron star surface while they all have limb-darkening profiles (e.x. Pavlov et al. 1994). If I consider limb-darkening effect only (and ignore the magnetic beaming), the effect is associated with the angle between the emission and the surface normal, θ_n. For a specific region with effective temperature T_{eff} on neutron star surface, with $I_0 = $ constant for normalization, and the limb-darkening beaming pattern:

$$f(\theta_n) = (1 - \xi \times (1 - \cos\theta_n)) \qquad (1)$$
$$0 \le \theta_n \le \pi/2$$

ξ is setting as the value 0.4 (e.x. Bowers and Deeming 1984). Figure 1 shows the beaming pattern $f(\theta_n)$ with $\xi = 0.4$.
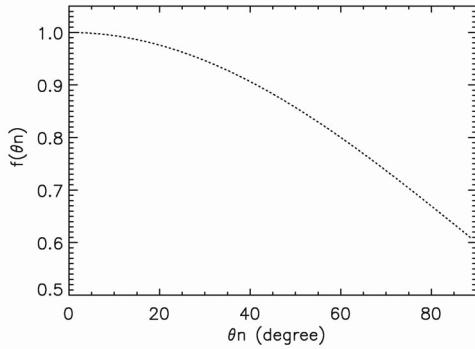

Fig. 1: Beaming pattern $f(\theta_n)$, equation (1), with $\xi = 0.4$.

Therefore,

total flux $\equiv \sigma T_{eff}^4$

$$= \int (\int I_v dv) \cos\theta_n d\Omega$$
$$= \int (\int I_0 f(\theta_n) B_v(T_{eff}) dv) \times \cos\theta_n d\Omega$$
$$= I_0 \frac{\sigma T_{eff}^4}{\pi} \underbrace{\int f(\theta_n) \times \cos\theta_n d\Omega}_{S_0(\theta_n) = constant}$$

Thus, for a emission photon with the angle θ_n', the limb-darkening effect make the specific intensity become

$$I_v(\theta_n') = I_0 f(\theta_n') B_v(T_{eff}) \qquad (2)$$

If sum over all frequency:

$$I = I_0 \frac{\sigma T_{eff}^4}{\pi} f(\theta_n') \qquad (3)$$

as a result of $f(\theta_n')$ is independent of frequency. In general, the limb-darkening profile is dependent with emission photon energy, while my work here is just an acceptable approximation.

2.4 The observed photon number

Photons are observed in X-ray observations. To model the light curves, then calculated the pulse fraction, the theoretical calculation of observed photon number flux are needed.

Recall that (for instance, Rybicki & Lightman 1979, p.146)

$$\frac{I_v}{v^3} = \text{Lorentz invariant} = \frac{I_v'}{v'^3} \qquad (4)$$

and

$$\frac{v'}{v} = \sqrt{1 - \frac{2M}{R}} \qquad (5)$$

where I is the intensity, v is the frequency and the *primed notations* represent the physical quantities measured by the distant observer.

Combine these equations (4), (5) and Planck functions:

$$T' = \sqrt{1 - \frac{2M}{R}} T$$

and

$$B_v'(T') = (\sqrt{1 - \frac{2M}{R}})^3 B_v(T)$$

For the blackbody radiation observed by a distant observer with the frequency band (v_1', v_2')

and characteristic temperature T', the observed photon number flux can be written as

$$\iint_{\nu'_1}^{\nu'_2} \frac{f \times B'_\nu(T')}{h\nu'} d\nu' d\Omega'$$

$$= (\frac{R}{r_0})^2 (1 - \frac{2M}{R})^{3/2} (\frac{M}{R})^2 \qquad (6)$$

$$\times \int_0^{2\pi} \int_0^{X_{max}} \int_{\nu_1}^{\nu_2} \frac{f \times B_\nu(T)}{h\nu} d\nu X' dX' d\phi'$$

where $\nu'_1 = \sqrt{1 - \frac{2M}{R}}\nu_1$, $\nu'_2 = \sqrt{1 - \frac{2M}{R}}\nu_2$, and $X' = b/M$, b is the impact parameter.

3 Constraining inclination and viewing angles of neutron stars from their X-ray thermal emission

A rough estimation of the inferred emitting area can be determined from observation results (e.x. see Table 1). For the case of X-ray dim isolated neutron stars, whose spectra has only one thermal component, I regard those components as the contribution of the hot spots by the hint of their inferred emitting areas are similar to those of the TH components. For example, by the temperatures and fluxes of the two blackbody components of PSR 0656+14 spectrum, Greiveldinger (1996) estimated a neutron star with radius 14^{+12}_{-1} km and high temperature emitting area is $2.5^{+7.9}_{-1.7} \times 10^{11}$ cm^2.

In this picture, by inputting these temperature parameters into the numerical calculations and adjusting the mass-to-radius ratio, the angular size of the hot polar caps, and the α, ζ angles can be picked up by the observational constraints: such as the observed flux (in units of $erg/sec/cm^2$) and pulse fraction, which is defined as the ratio between the number of counts above the DC level and the total number of counts in

light curve.

Consider a neutron star with following observational features:

(1) One spectral component: TH component, with fitting temperature T_h and flux F_h.

(2) Period P; Pulsed fraction F%.

Next I follow the steps to determine the geometry:

(1) Give the specific values of the two free parameters: the mass-to-radius ratio and the angular size of the hot polar cap.

(2) Apply the model with the hot pole temperature T_h.

(3) Give α and ζ, calculate the average observed flux and pulsed fraction after a spin period (which mimic to that what I observed is the "phase-averaged" property).

(4) Repeat (3) for different α and ζ.

(5) Find out the (α, ζ) set that produce flux $\sim F_h$ and pulse fraction "F%".

(6) Repeat (2)~(5) by changing different mass-to-radius ratio and hot spot size.

It is convenient to plot the results of step (6) in the parameter space, (α, ζ), for each mass-to-radius ratios and angular size of the hot spots.

As an illustration, I present how to search for the possible geometry of the source RX J0806.4-4123. RX J0806.4-4123 has only one thermal component in its spectrum. Some of the observational properties are shown in table 1.

Figures 2~4 show the contours (in parameter space, α-ζ plane) of computed flux and computed pulsed fractions with different mass-to-radius ratio (M/R = 0.01, 0.2, 0.3 for figures 2, 3, 4, respectively. The case for M/R = 0.1 is not shown

but *I will still mention its behaviors in the following discussions.*) and hot spot size. The computed flux were calculated in 0.1-2.4 keV band and divided by the observed flux, 28.8×10^{-13}, for convenience. The computed pulsed fraction was calculated in the energy band of 0.12-1.2 keV. Next, for each mass-to-radius ratio and hot spot size, I overlap the contours to search for the possible geometry,

Table 1: Observational properties of RX J0806.4-4123

Best Fit Temperature (eV)	Distance (pc)	Observed Flux (erg/sec/cm²)
95.6 (1)	100 (2)	$28.8^{+0.2}_{-0.2} \times 10^{-13}$ (1) (0.1-2.4 keV)
Inferred Emitting Area (cm²)	Pulsed Fraction	Period (second)
4×10^{10} [a]	6.2±1% (4) (0.12-1.2 keV)	11.371 [b]

(1) Haberl et al. (2004); (2) Haberl (2003); (3) Haberl (2004); (4) Haberl and Zavlin (2002)

[a] $A\sigma T^4 = 4\pi d^2$((bolometric flux)
A: inferred emitting area; d: distance to the source

[b] canonical polar cap size= $\sqrt{\dfrac{\Omega R}{C}}$ =0.004 ~ 0.25°

Ω: angular frequency of the neutron star;
R: the neutron star radius, set to be 10^6 cm;
C: speed of light

Table 2 : Observational properties of RX J0420.0-5022

Best Fit Temperature (eV)	Distance (pc)	Observed Flux (erg/sec/cm²)
44.8 (1)	100 (2)	$4.8^{+0.3}_{-0.3} \times 10^{-13}$ (1) (0.1-2.4 keV)
Inferred Emitting Area (cm²)	Pulsed Fraction	Period (second)
….	12% [a] (3) (0.12-0.7 keV)	3.454 [b]

(1) Haberl et al. (2004); (2) Haberl (2003); (3) Haberl (2004)

[a] single peak; no reported error bar.
[b] canonical polar cap size ~0.008 ~ 0.45°

Table 3 : Observational properties of RX J0720.0-3125

Best Fit Temperature (eV)	Distance (pc)	Observed Flux (erg/sec/cm²)
84.3 (1)	100 (2)	1.19×10^{-11} [a] (1) (0.1-2.4 keV)
Inferred Emitting Area (cm²)	Pulsed Fraction	Period (second)
1.4×10^{11}	11% [b] (3) (0.12-1.2 keV)	8.391 [c]

(1) Haberl et al. (2004); (2) Haberl (2003); (3) Haberl (2004)

[a] no reported error bar.
[b] single peak; no reported error bar.
[c] canonical polar cap size ~ 0.005 ~ 0.29°

that is, the intersection of the flux contour with value ~1 and pulsed fraction contour with value ~6%. For example, the upper right figure of figure 4.6 shows the overlap contours for the case of M/R equal to 0.1 and hot spot size is 22 times of the canonical polar cap size. The possible range for α and ζ is about 60° and 0~5°, respectively. Because of the symmetry of α and ζ in equation (4.1) of PFC's paper, the possible range also falls in the region α= 0~5° and ζ ~ 60°. I will not repeat this point hereafter.

The upper left figure of figure 5 show the regions of different characteristics of pulse profiles. For neutron stars with α, ζ falling in the "single peak region", such as point A, their light curves show single peak profile. The light curves for point A (α=20°, ζ=10°) and B (α=70°, ζ=60°) in the upper right figure are plotted in the lower left and lower right corner respectively.

Figure 6 shows the pulsed fraction contours in figure 2~4. Note that the contour of computed pulsed fraction varies very little (the right figures for same mass-to-radius ratio), on the other hand, the contour of computed observed flux varies obviously (the left figures for same mass-to-radius ratio). These behaviors also shown in other cases, RX J0420.0-5022 and RX J0720.4-3125, I'll mention this point later. In this way, the possible range is dominated by the behavior of the pulsed fraction because *one can always expect a suitable hot spot size would produce the required model flux contour to overlap the pulsed fraction contour*. From figure 2~4, the suitable hot spot sizes for different mass-to-radius ratios are summarized in table 4:

Table 4: constraints of hot spot size for RX J0806.4-4123

mass-to-radius ratio	suitable hot spot sizes (in unit of canonical polar cap size)
0.01	≥ 13
0.1	13-29
0.2	13-15
0.3	< 12

Figure 7 show the sum of the pulsed fraction contours of the value 6% for each mass to radius ratio in figure 6. The possible (α, ζ) regions roughly equal to the sum of these contours in figure 7 according to the previous discussion.

The dots in figure 7 represent 117 radio pulsar geometry reported by Rankin (1993). According to his research, the viewing angles and inclination angles roughly following the line of α ≈ ζ because the angle between the viewing angle and the inclination angle is not too large. Comparing the dots and contours in figures 7, apparently, the result of the method I used shows relative large possible geometry regions in the parameter space. If I consider that a typical neutron star with mass-to-radius ratio about 0.2~0.3, the region between the contour of 0.2 and 0.3 mass-to-radius value in figure 7 shows that the α and ζ angle are different form each other when α is large. However, the pulse profile of RX J0806.4-4123 shows single peak, therefore, the preferred region thus falls in the "single pulse region" indicated in figure 5 and shows no apparently different distribution with those of radio pulsars (the dots in figure 7).

For RX J0420.0-5022 and RX J0720.4-3125, their geometry can be inferred in the same way (see table 2 and 3, figures 8 and 9). The results for these two radio-quiet pulsars also have no strong evidence for the different geometry behavior between radio pulsars and themselves.

4 Summary

In this paper, by the motivation of neutron star with thermal X-ray emission, I assumed blackbody radiation from the surface of neutron stars and computed the model spectra and light curves. I view beaming effect as a modification of the strength of the radiation - a "modified blackbody radiation"($I_\nu = f(x) \times \dfrac{2\nu^2}{C^2} \dfrac{h\nu}{e^{h\nu/kT}-1}$, $f(x)$ comes from beaming effect). By using observational result, the best fit temperature(s), as input parameter, then search for the geometry (the inclination angle and the viewing angle) that produce consistent pulse fraction and observed flux. My computed result depends on the beaming pattern I use, as discussed in section 2.3, and I ignore the effect of neutron hydrogen absorption.

The inferred possible geometry range in this work is broad in the α-ζ plane and one cannot tell if the distribution for radio-quiet neutron stars and radio pulsars are different. However, the results help to gain some insight:

(1) If the observational pulse profile shows single peak, the possible geometry of the source narrows down to the *single peak region* in the α-ζ plane.

(2) If the α angle is similar to the ζ angle (i.e. α ~ ζ) for the radio-quiet neutron star source, just like the behaviors of radio pulsars, then I can constraint the hot spot size for different mass-to-radius ratio. For example, for the source RX J0806.4-4123, according to figures 2~4, the inferred possible hot spot sizes, for the case of α ~ ζ, are listed in table 5 (*c.f.* table 4).

To investigate possible reasons of the difference between the radio-quiet neutron stars and radio pulsars, more samples of radio-quiet neutron stars with known inferred possible α and ζ angle are needed in the future. Besides, more powerful methods are desired for determining or constraining the possible geometry ranges.

Table 5 : constraints of hot spot size for RX J0806.4-4123 for the case of α ~ ζ

mass-to-radius ratio	inferred hot spot sizes (in unit of canonical polar cap size)
0.01	≤ 18
0.1	13-25
0.2	13-15
0.3	< 12
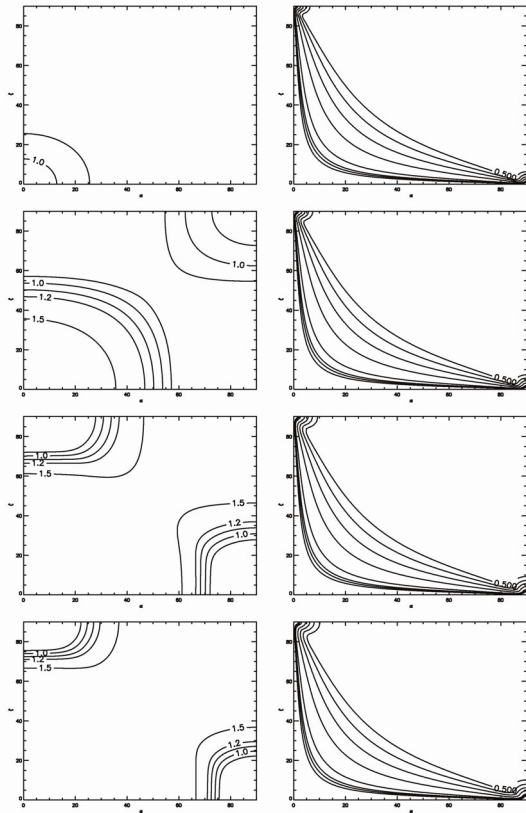
Fig. 2: Contours of computed RX J0806.4-4123 flux (left, values of contours ({flux/28.8×10^{-13}}) equal to {0.9, 1.0, 1.1, 1.2, 1.5}) and model pulsed fraction (right, values of contours equal to {0.05, 0.06, 0.07, 0.1, 0.2, 0.3, 0.4, 0.5}) for the case of mass-to-radius ratio equal to 0.01. The hot spot size equals to 13,18,25,28 times the canonical polar cap sizes for each row figures from up to down, respectively.   ↑

Fig. 4: Contours of computed RX J0806.4-4123 flux (left, values of contours ({flux/28.8(10-13)}) equal to {0.9, 1.0, 1.1, 1.2, 1.3}) and model pulsed fraction (right, values of contours equal to {0.05, 0.06, 0.07, 0.1, 0.2}) for the case of mass-to-radius ratio equal to 0.3. The hot spot size equals to 10,11,12,13 times the canonical polar cap sizes for each row figures from up to down, respectively.   →
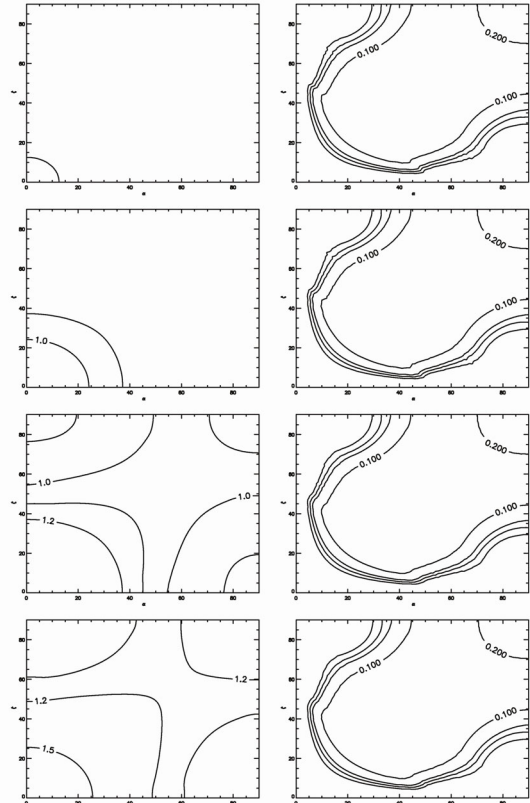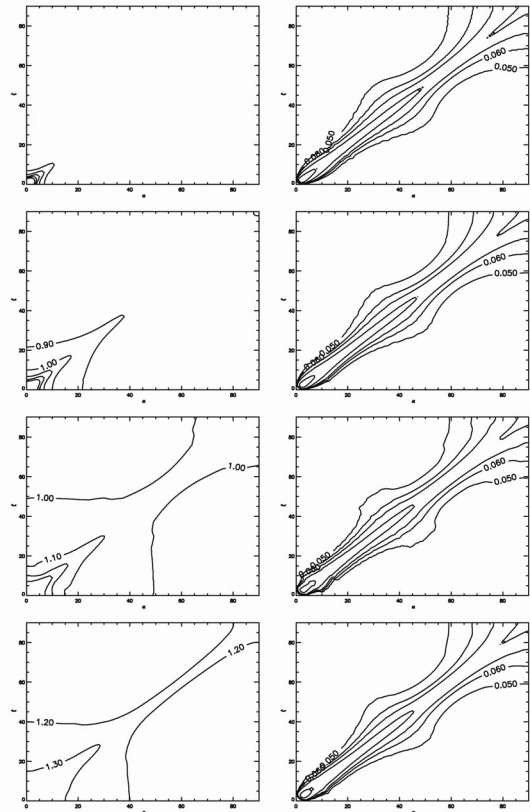

Fig. 3: Contours of computed RX J0806.4-4123 flux (left, values of contours ({flux/28.8×10^{-13}}) equal to {0.9, 1.0, 1.1, 1.2, 1.5}) and model pulsed fraction (right, values of contours equal to {0.05, 0.06, 0.07, 0.1, 0.2}) for the case of mass-to-radius ratio equal to 0.2. The hot spot size equals to 12,13,15,16 times the canonical polar cap sizes for each row figures from up to down, respectively.
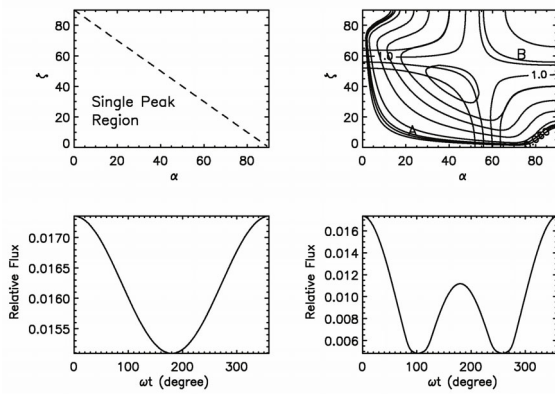
Fig. 5: The light curve behaviors and the overlap of the computed RX J0806.4-4123 flux and pulsed fraction for the case of mass-to-radius ratio equal to 0.1 and hot spot size equal to 22 times the canonical polar cap size. See text for details.
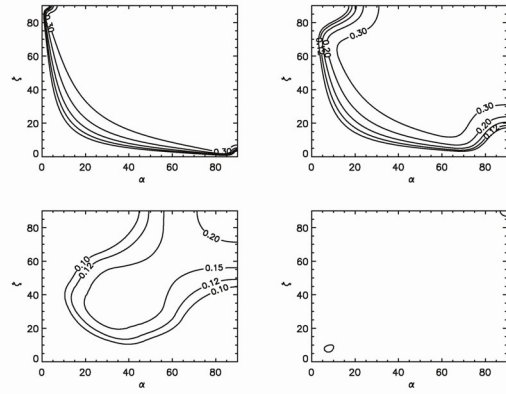
Fig. 8: Contours of computed RX J0420.0-5022 pulsed fraction for mass-to-radius ratio 0.01 (upper left), 0.1 (upper right), 0.2 (lower left) and 0.3 (left right). Contours values equal to {0.1, 0.12, 0.15, 0.2, 0.3}. There is no possible geometry region for the case of the mass-to-radius ratio equal to 0.3.
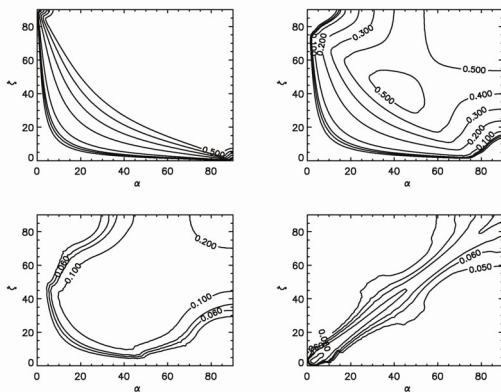
Fig. 6: Contours of computed RX J0806.4-4123 pulsed fraction for mass-to-radius ratio 0.01, 0.1, 0.2, 0.3 for upper left, upper right, lower-left, left right, respectively.
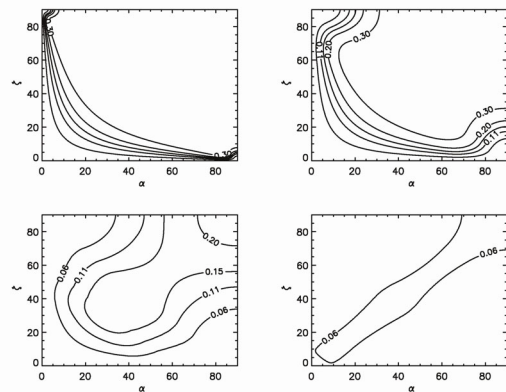
Fig. 9: Contours of computed RX J0720.4-3125 pulsed fraction for mass-to-radius ratio 0.01 (upper left), 0.1 (upper right), 0.2 (lower left) and 0.3 (left right). Contours values equal to {0.06, 0.11, 0.15, 0.2, 0.3}. There is no possible geometry region for the case of the mass-to-radius ratio equal to 0.3.
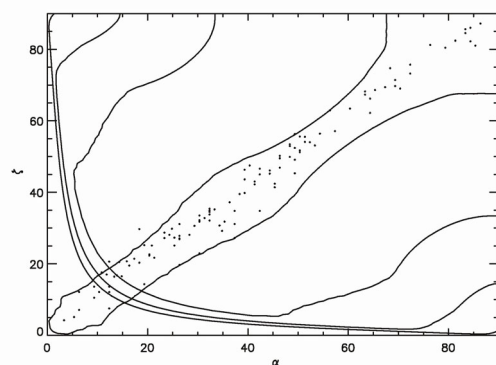
Acknowledgment

Fig. 7: Sum of computed RX J0806.4-4123 pulsed fraction contours of the value 6%. The mass-to-radius ratios are 0.01, 0.1, 0.2 and 0.3 from outer most to inner most curves. The dots represent 117 radio pulsar geometries reported by Rankin (1993).

Reference

Becker, W., and Trumper, J., 1997, *A&A*, 326, 682

Bowers, R .L., and Deeming, T., 1984, *Astrophysics I: stars*, Boston: Jones and Bartlett publishers

Chang, H. K., 2001, *Chinese Journal of Physics*, 39, NO.4

Gonthier, P. L., and Harding, A. K., 1994, *ApJ*, 425, 767

Greiveldinger, C. et al., 1996, *ApJ*, 465, L35

Haberl, F. and Zavlin, V. E., 2002, *A&A*, 391, 571

Haberl, F., 2003, *astro-ph/0302540*

Haberl, F., 2004, *Mem. S.A.It.*, 75, 454

Haberl, F., Motch, C., Zavlin, V. E., Reinsch, K., Gansicke, B. T., Cropper, M., Schwope, A. D., Turolla, R., and Zane, S., 2004, *A&A*, 424, 635

Hurley, K., 1999, *astro-ph/9912061*

Israel, G., Mereghetti, S., Stella, L., 2001, *astro-ph/0111093*

Kaspi, V. M., Roberts, M. S. E. and Harding, A. K., 2004, *astro-ph/0402136*

Luca, A. D., Mereghetti, S., Caraveo, P. A., Moroni, M., Bignami, C. F., 2004, *A&A*, 418, 625

Mereghetti, S., Chiarlone, L., Israel, G. L., Stella, L., 2002, *astro-ph/0205122*

Misner, C.W., Thorne, K. S., and Wheeler, J. A., 1977, *Gravitation*, San Francisco; Freeman

Özel, F., 2001, *ApJ*, 563, 276

Pavlov, G. G., Shibanov, Yu. A., Ventura, J., and Zavlin, V. E., 1994, *A&A*, 289, 837

Pavlov, C. G, Garmire, G. P., 2001, astro-ph/0112322

Pechenick, K. R., Ftaclas C., and Cohen J. M. (PFC), 1983, *ApJ*, 274, 846

Popov, S. and Turolla, R., 2003, *astro-ph/0312369*

Rankin, J. M., 1993a, *ApJ*, 405, 285

Rankin, J. M., 1993b, *ApJS*, 85:145

Rybicki, G. B., and Lightman A. P., 1979, Radiative processes in astrophysics, New York: Wiley. Treves, A., Turolla, R., Zane, S., and Colpi, M., 2000, PASP, 112, 297

Wasserman, and Shapiro, 1983, *MNRAS*, 327, 1036

Zavlin, V. E., Pavlov, G. G., and Shibanov, Yu. A., 1996, *A&A*, 315, 141

Zavlin, V. E., Pavlov, G. G., 2002, *astro-ph/0206025*